

Elastic, inelastic, and one-neutron transfer angular distributions of ${}^6\text{Li} + {}^{120}\text{Sn}$ at energies near the Coulomb barrier

V. A. B. Zagatto ^{1,*}, M. Gómez-Ramos,² L. R. Gasques ³, A. M. Moro,² L. C. Chamon ³, M. A. G. Alvarez ²,
V. Scarduelli ³, J. P. Fernández-García,² J. R. B. de Oliveira ³, A. Lépine-Szily,³ and A. Arazi ⁴

¹*Instituto de Física da Universidade Federal Fluminense, 24210-346, Niterói, Brazil*

²*Departamento FAMN, Universidad de Sevilla, Apartado 1065, 41080 Sevilla, Spain*

³*Instituto de Física da Universidade de São Paulo, 05508-090, São Paulo, Brazil*

⁴*Laboratorio TANDAR, Comisión Nacional de Energía Atómica, Av. Gral. Paz 1499, BKNA1650 San Martín, Argentina*



(Received 27 May 2022; accepted 6 July 2022; published 25 July 2022)

The elastic scattering, first 2^+ and 3^- target inelastic excitation and one neutron pickup angular distributions for the ${}^6\text{Li} + {}^{120}\text{Sn}$ reaction have been measured for three bombarding energies (19, 24, and 27 MeV). Data have been analyzed through coupled-channel calculations and continuum-discretized coupled-channel calculations extended to include target excitation. In general, both theoretical models give a reasonable description of the data. For the elastic and inelastic angular distributions taken at $E_{\text{lab}} = 24$ and 27 MeV, the continuum-discretized coupled-channel results are slightly better in comparison to the coupled-channel predictions. For the elastic and inelastic angular distributions measured at $E_{\text{lab}} = 19$ MeV, the effect of the break-up channel seems to be quite important. At this energy, the elastic scattering data can be well explained by coupled channel calculations in which a strong absorptive optical imaginary potential is considered. In particular, the continuum-discretized coupled-channel theoretical results provided the best description of the 3^- excitation data at 19 MeV.

DOI: [10.1103/PhysRevC.106.014622](https://doi.org/10.1103/PhysRevC.106.014622)

I. INTRODUCTION

The nuclei of our present universe have been generated from a series of reactions that took place in different environments, from the interior of stars to supernovae. The series of long chains of reactions that generated all of these nuclei initiated with hydrogen, helium, and lithium isotopes created in the primordial nucleosynthesis [1]. The correct determination of the abundance of these initial nuclei is still of paramount importance for astrophysics and its correlated fields, since they consist in a probe to cosmological models and their parameters [2]. Although the experimental abundances of deuterium and ${}^3\text{He}$ are consistent with theoretical models [3], there is a great disagreement between experimental observations and theory for ${}^6\text{Li}$ and ${}^7\text{Li}$ isotopes [4]. For ${}^7\text{Li}$, this fact is known as *the lithium problem* [5], and some authors claim the existence of a *second lithium problem* related to ${}^6\text{Li}$ [6].

The ${}^6,7\text{Li}$ primitive abundances are based on the observation of low metallicity stars (given by the presence of elements heavier than helium) located in the halo of our galaxy. In these stars, the lithium abundance displays the so-called Spite plateau [7,8], indicating that their abundance is independent of the metallicity of the star. The Spite plateau indicates that the deposited lithium was originated on the primordial nucleosynthesis and was not depleted from the surface of such stars. Even though the ${}^6\text{Li}$ isotope has been poorly generated in the

primordial nucleosynthesis, its importance is enormous, since ${}^6\text{Li}$ participates on several reactions that have contributed to the synthesis of the elements present in our universe. For instance, the $\alpha({}^2\text{H}, \gamma){}^6\text{Li}$ and ${}^6\text{Li}(p, \alpha){}^3\text{He}$ reactions [9], that respectively create and annihilate the ${}^6\text{Li}$ isotope, can have a great impact in the deuterium and ${}^3,4\text{He}$ abundances, which in turn played a central role in the primordial nucleosynthesis scenario.

The calculations of the initial abundance of the elements in our earlier universe depends on the nuclear cross sections of the reactions which occurred there. If one wants to properly describe such reactions and their network, it is of ultimate importance to understand all the mechanisms that a given nucleus may undergo. In this sense, reactions involving lithium isotopes can be challenging, since they can undergo the break-up (BU) process. Both lithium isotopes may be described by an α core, associated with a valence particle (${}^2\text{H}$ in the case of ${}^6\text{Li}$ and ${}^3\text{H}$ for the ${}^7\text{Li}$), that is weakly bound to the α (1.47 MeV for ${}^6\text{Li}$ and 2.47 MeV for ${}^7\text{Li}$). The possibility of the projectile to break-up during its interaction with other nuclei gives rise to several new paths for the nuclear reaction mechanism to occur. For instance, in the fusion process exists the possibility that all fragments are captured by the target (complete fusion), or just one of them to be fused with it (incomplete fusion). The role played by the BU process in the fusion remains a topic of great interest in the field of nuclear physics [10–12]. The BU may also have an impact on other several reaction channels, such as elastic [13,14], neutron transfer [15], and charged particle transfer [16].

*vzagatto@id.uff.br

Understanding the complexity involving the BU process in stable weakly bound nuclei consists in a first step to understand the same process in exotic nuclei. However, technical difficulties in producing intense exotic beams result in yields with very low statistics when compared to experiments performed with stable beams. For this reason, the uncertainties of the corresponding cross sections are usually quite large, sometimes making it very difficult to properly study some particular feature of exotic nuclei. On the other hand, nuclear reactions performed with high-intensity stable beams are excellent probes for testing different theoretical models (i.e., continuum-discretized coupled channels (CDCC) [17], adiabatic approximation [18], and Faddeev-AGS equations [19]). In our previous works, such effects have been studied in ${}^7\text{Li}$ [13,20] and ${}^{10}\text{B}$ [21–24]. In addition, the elastic scattering data of the ${}^6\text{Li} + {}^{120}\text{Sn}$ reaction has been previously published [25], although the effect of BU was not discussed in that work.

Theoretically, the BU process is modeled considering the projectile as a composite of two inert particles, the core and its valence. Such approximations are valid in reactions that involve deuterons, but for more complex particles some extensions need to be incorporated in order to take into account the more intricate processes that such particles may undergo. Thus, theoretical models which incorporate the collective excitation of the core subsystem have been developed [26–28]. Even being successfully applied, such models have limitations to describe the possible excitations of the projectile, while neglecting the excited states of the target. In such models, the inclusion of the effects generated by the excitations of the target is done in an effective way through the incorporation of a fragment-target optical potential. Particularly, target excitation was included in CDCC calculations by the Kyushu-Pittsburg group in the 1980s [29], and have recently received renewed attention [30,31]. This model, which is an extension of the CDCC method, is considered in the present paper. It is worth mentioning that this method was already adopted to describe the inelastic scattering cross sections for the ${}^6\text{Li} + {}^9\text{Be}$ [32] and ${}^6\text{Li} + {}^{144}\text{Sm}$ [33] reactions.

The work is organized as follows. In Sec. II, the experimental setup is presented and a short briefing about the data reduction is made. Section III brings the results of the theoretical calculations and their comparison with data. The closing remarks and conclusions are presented in Sec. IV.

II. EXPERIMENTAL MEASUREMENT AND DATA REDUCTION

The present work was carried out at the 8 MV tandem accelerator at the LAFN-USP laboratory. The ${}^6\text{Li}$ beam was produced by an MC-SNICS ion source using lithium oxide cathodes. Two enriched ${}^{120}\text{Sn}$ ($\approx 99\%$) targets have been used along the experiment. One target was made by the evaporation of ${}^{120}\text{Sn}$ isotope, while the other target had also a thin ${}^{197}\text{Au}$ backing used for normalization purposes. The accelerator delivered beams with three different bombarding energies: 19 MeV, 24 MeV, and 27 MeV. The energy loss of the ${}^6\text{Li}$ beam passing through the targets was about 0.1 MeV. The typical beam intensity varied from some tens to some hundreds of nA, and was chosen depending on the angular position of

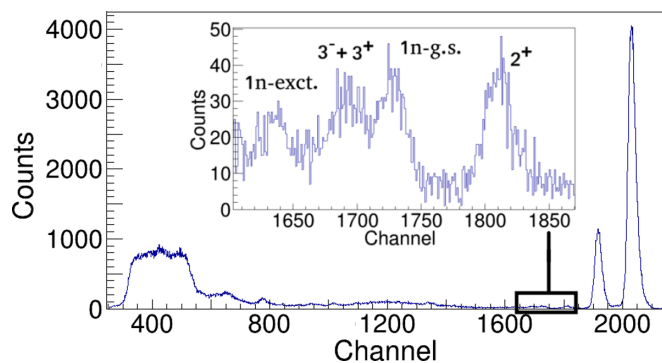


FIG. 1. Single-channel spectrum taken with a detector at $\theta_{\text{lab}} = 105^\circ$ placed on the SATURN array. The corresponding bombarding energy is 24 MeV. Elastic scattering yields from tin and gold nuclei may be seen in the right side of the figure. In the inset, it is possible to better visualize the inelastic and one-neutron transfer processes. See text for further details.

the detectors (always avoiding too high count rates that could damage them).

The measurements were performed using two different detector arrays: SATURN (silicon array based on telescopes of USP for reactions and nuclear applications) and STAR (silicon telescopes array for reactions). The SATURN array was composed by a set of nine single thick silicon surface barrier detectors mounted on a rotating arm. Each detector was 5° apart from the next, covering an angular region of 45° . The STAR array consists of a ΔE - E telescope composed by a single sided silicon strip detector (segmented in 16 vertical strips) with an average thickness of $20\ \mu\text{m}$ associated to an E detector with approximately $1000\ \mu\text{m}$ thickness, covering an angular region of about 35° . Its center was positioned at $\theta_{\text{lab}} \approx 140^\circ$. In order to limit its angular coverage in its polar angle, a tantalum mask has been placed in front of the detector. Although both SATURN and STAR arrays are complementary to each other, the advantage of using a large area telescope detector is related to the possibility of identifying the entrance particles by their mass and charge.

Figure 1 shows a typical spectrum acquired with a single silicon detector of SATURN, placed at $\theta_{\text{lab}} = 105^\circ$ with bombarding energy of 24 MeV, impinging on a ${}^{120}\text{Sn}$ target with ${}^{197}\text{Au}$ backing. The most intense peak on the right side of the spectrum corresponds to the ${}^6\text{Li}$ particles elastically scattered on the ${}^{197}\text{Au}$ backing, while the peak placed at its left is the elastic scattering of the beam interacting with the ${}^{120}\text{Sn}$ target. A clear bump on the left side of the spectrum, which is likely correlated to reaction mechanisms such as BU and fusion, can also be observed. The inset displays the figure using an expanded scale to allow a better visualization of the inelastic and transfer yields. From right to left, the identified processes are (1) inelastic scattering corresponding to the 2^+ excited state of the ${}^{120}\text{Sn}$ target ($E^* = 1.171\ \text{MeV}$); (2) one-neutron transfer to the low-lying states of ${}^{119}\text{Sn}$ ($1/2^+\text{g.s.}$, $3/2^+$ with $E^* = 0.024\ \text{MeV}$ and $11/2^-$ with $E^* = 0.089\ \text{MeV}$); (3) inelastic scattering of the 3^- excited state of the ${}^{120}\text{Sn}$ target ($E^* = 2.400\ \text{MeV}$) and 3^+ excited resonant state of the ${}^6\text{Li}$ projectile ($E^* = 2.186\ \text{MeV}$); (4) one-neutron transfer to the

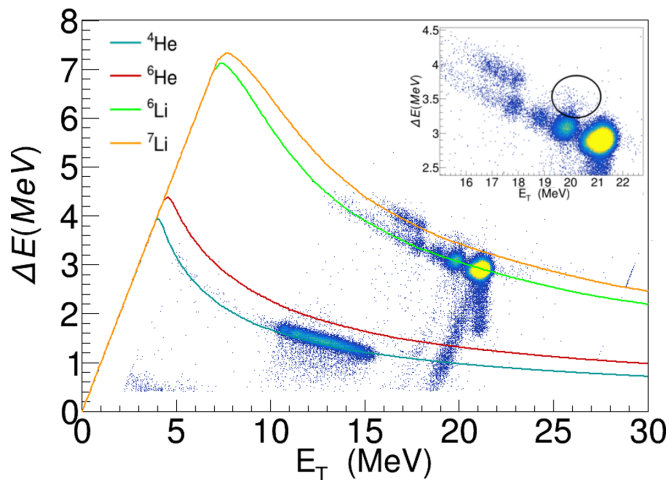


FIG. 2. $(\Delta E-E_T)$ spectrum for $E_{\text{lab}} = 24$ MeV and scattering angle of $\theta_{\text{lab}} = 150.1^\circ$. The colored solid lines represent theoretical calculations of energy loss in function of the total energy. The black circle of the inset shows $1n$ -transfer events occurring in the ^{197}Au backing. See text for further details. The energy loss calculations followed the method explained in Ref. [34].

excited state of ^7Li and excited states of ^{119}Sn (from $7/2^+$ with $E^* = 0.787$ MeV to $5/2^+$ with $E^* = 1.354$ MeV).

A typical $\Delta E-E_T$ spectrum obtained with the STAR array is shown in Fig. 2. The ^6Li beam energy was 24 MeV and the spectrum corresponds to a strip located at $\theta_{\text{lab}} = 150.1^\circ$. In this figure, it is possible to observe different ejectiles emerging from the target. The solid lines represent the energy loss calculations of the corresponding nuclei as a function of the total energy [34]. As expected, one may notice two intense peaks corresponding to the elastic scattering in ^{120}Sn target and ^{197}Au in the ^6Li region represented by the green line. One may also observe two groups of states in the ^7Li region (orange line), which are separated from each other by about 2 MeV (see the inset of Fig. 2). The yields contained in the black circle of the inset are coming from the $1n$ transfer events occurring between the projectile and the ^{197}Au backing. Besides being in the correct energy position of the spectrum, this was also confirmed by the absence of such events in the runs performed with a pure ^{120}Sn target. From Fig. 2, one may observe a great number of α particle events. Also, some events corresponding to the formation of ^6He can be seen. Although rare, such observed yields might be related to a two-step transfer process, where a sequential proton pickup followed by a neutron stripping (or vice versa) takes place. Alternatively, the formation of ^6He nuclei can be associated to the single-charge exchange process, in which the interaction of protons and neutrons are described in terms of the exchange of mesons (i.e., a proton becomes a neutron by emitting a π^+ meson).

In Ref. [25], only the elastic scattering angular distributions acquired with the SATURN array were presented and not all data sets have been published. In the present paper, all elastic scattering and other reaction channels, which were acquired with both SATURN and STAR arrays, are presented. Regarding the data acquired with the STAR array, the corresponding cross

sections were obtained averaging the corresponding yields of every three consecutive strips, as the angular step of the first stage ΔE detector is quite small ($\approx 2.2^\circ$).

III. DISCUSSION AND THEORETICAL FRAMEWORK

After performing the data analysis, it was possible to obtain the angular distributions of the elastic channel, the 2^+ ($E^* = 1.171$ MeV) and 3^- ($E^* = 2.400$ MeV) excited states of ^{120}Sn target, and two transfer angular distributions resulting from the one neutron pickup process. The observed channels in the present experiment are similar to those observed in Refs. [13,21,35]. As a first approach, a coupled channel (CC) calculation was performed considering the São Paulo potential (SPP) [36–38] as the bare nuclear interaction. The excited states of the ^{120}Sn target (2^+ and 3^-) were included in the coupling scheme. The deformation lengths for the target excitation adopted in the calculations were: $\delta_2 = 0.64$ fm and $\delta_3 = 0.98$ fm. These deformation lengths have been obtained from the $B(E2)$ and $B(E3)$ values reported in Refs. [39,40] and [41]. The δ_2 value is compatible with those reported in [21], whereas the δ_3 value is compatible (considering the uncertainties) with that obtained from the $B(E3)$ value of [41]. The calculations were carried out using the FRESKO code [42]. Two different models were assumed for the imaginary part of the optical potential, as discussed below. Both real and imaginary potentials were deformed in the CC calculations.

Figure 3 shows the elastic scattering angular distributions measured with the SATURN (yellow circles) and STAR (blue squares) arrays. The black solid curves correspond to the results obtained with a Woods-Saxon (WS) internal imaginary potential ($W_0 = 50$ MeV, $r_0 = 1.0$ fm and $a = 0.2$ fm). As can be noticed, the difference between the theoretical and experimental results are quite large at $E_{\text{lab}} = 19$ MeV for scattering angles larger than 100° . This indicates that the BU may play an important role in the reaction mechanisms for the $^6\text{Li} + ^{120}\text{Sn}$ reaction at sub-barrier energies. For the $E_{\text{lab}} = 24$ MeV (27 MeV), the small discrepancies between the black curve and the data are more pronounced at forward (backward) angles.

In order to simulate the effect of the BU and other possible processes on the elastic channel, we have performed further calculations where the imaginary potential was considered as proportional to the bare real interaction $W(r) = N_i \times V(r)$. In the corresponding CC calculations, the N_i parameter value was adjusted to provide a satisfactory description of the elastic data. The dashed red lines presented in Fig. 3 were obtained considering $N_i = 1.2$, which results in a quite absorptive imaginary potential at the surface region. In this calculation, the angular distributions at $E_{\text{lab}} = 19$ MeV and 27 MeV are well reproduced by the theoretical results. At 24 MeV, the surface absorptive potential improves the agreement with the data at forward angles, but makes it worse it at the backward region. Even so, the differences between theory and experiment are not larger than 20% for the entire angular region. It is important to mention that the $N_i = 1.2$ value is significantly larger than that of $N_i \approx 0.78$, obtained from a systematical study of elastic scattering through optical model calculations with the SPP [43].

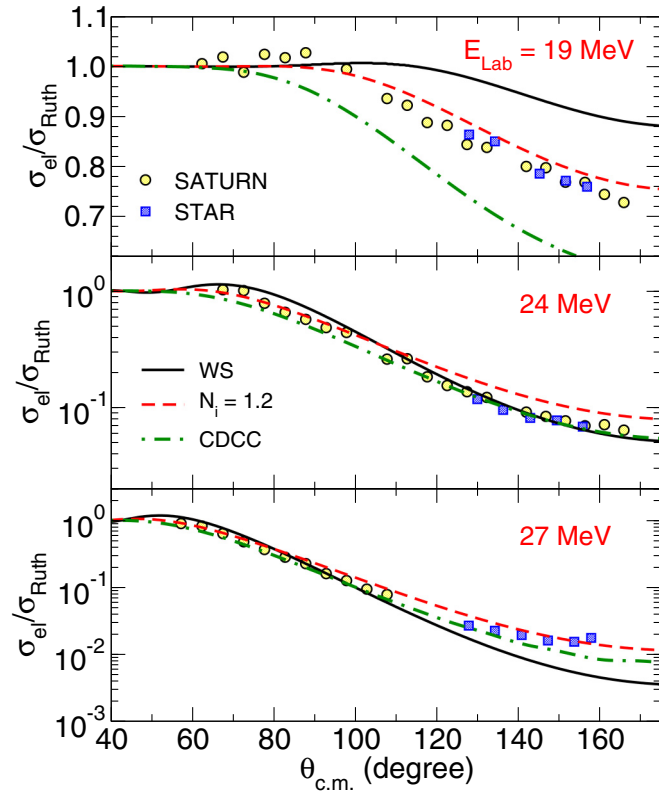


FIG. 3. Elastic scattering for the ${}^6\text{Li} + {}^{120}\text{Sn}$ reaction at 19, 24, and 27 MeV bombarding energies. The SATURN data are represented by the yellow circles and the STAR data are represented by the blue squares. The microscopical CC theoretical results obtained with the internal WS imaginary potential are presented as solid black lines. The dashed red lines correspond to CC calculations with strong surface absorption ($N_i = 1.2$). The dotted-dashed green lines show the results of the CDCC calculations.

The angular distributions for the ${}^{120}\text{Sn}$ 2^+ excited state are shown in Fig. 4. A comparison between the calculations with internal imaginary potential (solid black lines) and scaled SPP (dashed red lines) shows that the geometrical form of the imaginary potential has a weak effect on the 2^+ inelastic cross sections at $E_{\text{lab}} = 19$ MeV. Although differences of around 20% are present at the backward angular region, both curves describe reasonably well the average trend of the data. For the angular distributions taken at energies above the Coulomb barrier, the discrepancies between the two calculations are larger and can be noticed for all depicted scattering angles. In general, the results obtained with the internal imaginary potential are in better agreement with the data.

An inspection of Fig. 5 reveals the dependence of adopting quite different imaginary potentials for the 3^- inelastic angular distributions measured at $E_{\text{lab}} = 19$ MeV. Although the somehow poor description of the data obtained by adopting both imaginary potentials, the strongly surface absorptive imaginary potential results in a better agreement with the data. For $E_{\text{lab}} = 24$ MeV and 27 MeV, both solid black and dashed red lines describe, in average, both the trend and the strength of the data. It is worth mentioning that the 3^- cross

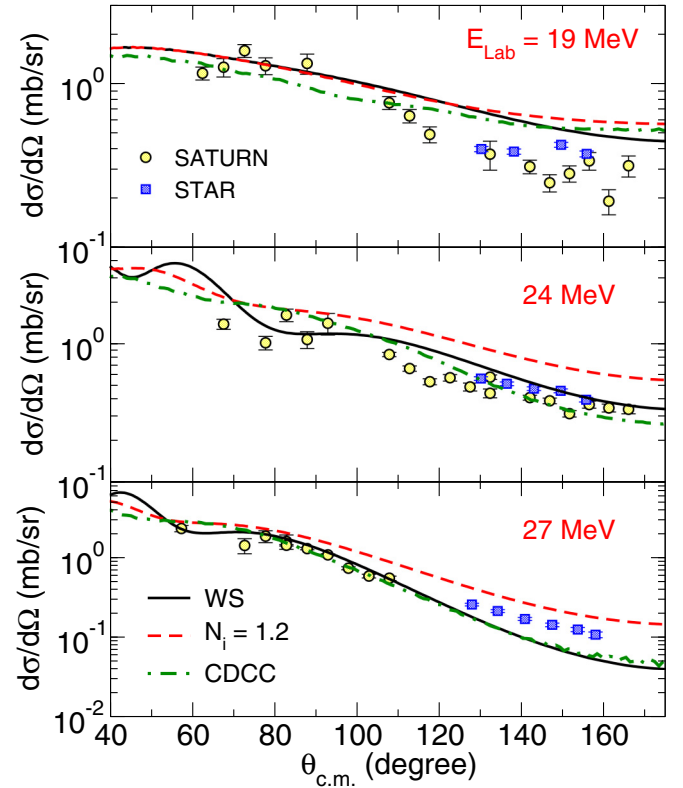


FIG. 4. The inelastic scattering angular distributions for the ${}^{120}\text{Sn}$ 2^+ ($E^* = 1.171$ MeV) excitation at $E_{\text{lab}} = 19, 24,$ and 27 MeV. The SATURN and STAR data are represented by the yellow circles and blue squares, respectively. The lines represent the results of the theoretical CC (internal WS and $N_i = 1.2$ imaginary potentials) and CDCC calculations.

sections can contain a contribution arising from the first 3^+ excited state of the ${}^6\text{Li}$ projectile at $E^* = 2.186$ MeV. Although this excitation energy is higher than the threshold for the breakup of the projectile into the $\alpha + {}^2\text{H}$ partition, it is expected that the probability of ${}^6\text{Li}$ surviving the collision is not null. Therefore, the discrepancy between the experimental data set and the theoretical results observed at the frontal angular region can be correlated to the contribution of the 3^+ resonant state of ${}^6\text{Li}$, which might be included on the experimental cross sections.

It would be reasonable to argue that the observed differences between the CC calculations and the corresponding data could emerge from the adopted $B(E2)$ and $B(E3)$ values. Such values have been taken from a series of different experimental measurements. Therefore, it is natural to expect that the reduced transition probabilities reported in Refs. [39–41] have an experimental uncertainty associated to them. To check the sensitivity of the CC results to the uncertainty associated to the $B(E\lambda)$ experimental values, we have performed some further calculations, varying these values and comparing the results with the measured angular distributions. Considering a 3σ experimental confidence interval allows a variation of about 10% on the reduced transition probabilities values. However, the adoption of this procedure does not result in a significant

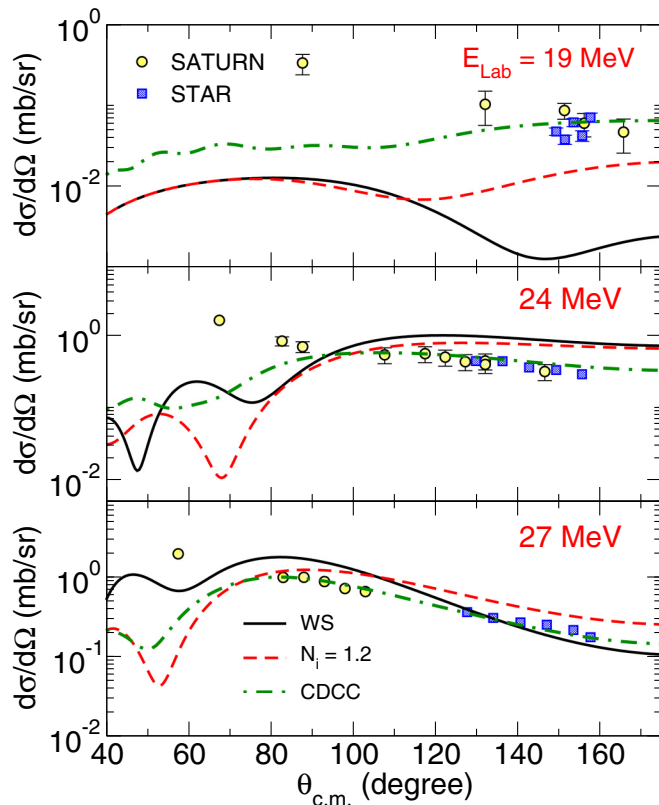


FIG. 5. The same as Fig. 4, for the excitation of the $^{120}\text{Sn } 3^- (E^* = 2.400 \text{ MeV})$ state.

improvement of the description of the elastic and inelastic angular distributions for the three bombarding energies.

In a recent work [13], the BU effect of the ^7Li projectile has been included in the CC scheme via a trivially equivalent local polarization potential (TELP). The TELP was obtained using the CDCC model in a separate calculation. The inclusion of BU has been demonstrated of paramount importance to properly describe the observed experimental angular distributions. In the present work, a different approach has been adopted to obtain the simultaneous description of the elastic and inelastic channels [31]. One advantage of adopting such procedure is related to the possibility of using the coupling potentials in order to treat the BU of the projectile and the collective states of the target simultaneously, avoiding the use of two distinct theoretical frameworks. Furthermore, the current approach allows to directly couple the inelastic channels of the target with the continuum of projectile (checking the effect of such coupling), which was not possible in our previous work.

The theory presented in [31] is based on writing the general Hamiltonian of the system as a sum of a term describing the relative motion between the projectile and target plus their internal Hamiltonians. The projectile Hamiltonian can be described as the sum of the kinetic energy and the potential energy between the core and valence particles (^4He and ^2H in the present case). The CDCC coupling potentials are obtained as the matrix elements between internal states of the projectile of the sum of the core-target and valence-target interactions. The model considers the breakup of the projectile

through CDCC, using a collective model to describe the target excitation. A rotor model is assumed for the target, and the fragment-target potentials are deformed as in standard CC calculations. Further details of these calculations can be found in the original reference [31].

It is expected that the BU process plays a bigger role in the case of ^6Li ($B = 1.473 \text{ MeV}$) than the one observed for the ^7Li ($B = 2.467 \text{ MeV}$) given its lower excitation energy necessary for breaking the projectile. In the present calculations, the ^6Li projectile has been treated as an inert ^4He core and a ^2H cluster, also assumed to be inert. Other BU modes of the projectile have been disregarded. To describe the continuum states of the ^6Li projectile, a Gaussian potential has been adopted to describe the α - d s wave, while a WS shape for the p and d waves has been chosen to reproduce the experimental excitation energy and width of the 3^+ resonance ($E^* = 2.186 \text{ MeV}$) of ^6Li . It is important to mention that, to avoid numerical convergence issues, the intrinsic 1^+ spin of the deuteron could not be considered and was set equal to 0^+ . Therefore, the ^6Li resonance has been considered as having its spin-parity equal to 2^+ . Conventional CDCC calculations (without target excitation) have been performed using the same potentials in order to check the importance of including the 1^+ deuteron spin. The difference between both CDCC calculations was negligible, validating the adopted theoretical approach. All the CDCC calculations have been performed considering the projectile excitation energy up to 11.5 MeV.

The core-target and valence-target potentials are important ingredients in the CDCC model. In the present work, the optical potential for the α - ^{120}Sn interaction was chosen as a standard SPP with $N_i = 0.78$ normalization for the imaginary part [43]. The deuteron interaction with the ^{120}Sn target was taken from the parametrization proposed in [44], without considering the spin-orbit potential. Both interactions (d/α - ^{120}Sn) have been deformed in order to take into account the coupling of the excited states of the target. The deformation lengths of the 2^+ and 3^- states of ^{120}Sn have once again been adopted as $\delta_2 = 0.64 \text{ fm}$ and $\delta_3 = 0.98 \text{ fm}$, respectively.

The continuum wave functions were generated using a transformed harmonic oscillator basis, which generated the continuum states for each partial wave (without deuteron spin $J = L = 0, 1, 2$) up to a certain maximum $d + \alpha$ energy, which was 12 MeV for the cases with beam energies at 24 and 27 MeV. This energy was chosen to maximize the number of states included in the calculations, while avoiding numerical divergence. Some tests varying this maximum energy showed convergence of the elastic and inelastic cross sections. For each partial wave, nine or ten states were resulting in roughly 30 states for the continuum. Since these states must be coupled to the three considered states of the target (g.s., 2^+ , and 3^-) this resulted in ≈ 90 states. As for the case of 19 MeV, it was found that the elastic cross section convergence required the inclusion of the $J = L = 3$ wave. A maximum energy of 12 MeV proved to be numerically unstable. As such, the maximum energy was reduced to 6 MeV and the states with $L = 3$ were included. This resulted in roughly eight states per partial wave, also leading to about 90 states.

The CDCC calculations considering the target excitation can be visualized in Figs. 3, 4, and 5 as dotted-dashed green

lines. The analysis of Fig. 3 shows that the elastic scattering angular distributions provided by the CDCC are in good agreement with the experimental data for $E_{\text{lab}} = 24$ and 27 MeV. However, for the angular distribution measured at 19 MeV, where the effect of BU is expected to be strong, the CDCC calculations underestimate the data. The inelastic data, displayed at Figs. 4 and 5, are reasonably well described by the CDCC calculations for all bombarding energies. In general, the agreement with the measured angular distributions is satisfactory, improving the description of the data with respect to the CC calculations based on a deformed projectile-target potential.

The discrepancy at 19 MeV between the CDCC calculation and the experimental elastic scattering data is rather puzzling, since the same calculations with the same parametrization of the optical potentials lead to good agreement at 24 and 27 MeV. Moreover, the inelastic channels are well reproduced for the three projectile energies. Further calculations show that a significant reduction of the imaginary part of the d - ^{120}Sn potential (by a factor of 0.25) allows for a better agreement with experimental data for the elastic scattering at 19 MeV, while keeping a reasonable agreement for the inelastic cross sections. It is difficult to find a reason for such a significant reduction in the potential. However, in [45], the study of the $^6\text{Li} + ^{209}\text{Bi}$ reaction at energies below the Coulomb barrier showed a reduction in the breakup of the deuteron for reactions involving ^6Li . Since deuteron breakup is one of the main processes that remove flux from the elastic channel in the deuteron-target interaction, a reduction in deuteron breakup due to the influence of the alpha particle may require a smaller imaginary potential. This is also consistent with the results obtained in the present work at 19 MeV.

Besides the elastic and inelastic yields, the one-neutron pickup transfer process, resulting in the ^7Li ejectile and the ^{119}Sn residual nucleus, has also been experimentally observed. Two peaks, containing the contribution of different states which can not be experimentally resolved, have been identified in the spectra. The first peak (named Peak 1) contains the first three low-lying states of ^{119}Sn ($1/2^+$ with $E^* = 0.000$ MeV, $3/2^+$ with $E^* = 0.024$ MeV and $11/2^-$ with $E^* = 0.089$ MeV). The second peak (named Peak 2), which has a larger width, is a combination of several excited states of ^{119}Sn ($7/2^+$ with $E^* = 0.787$ MeV, $3/2^+$ with $E^* = 0.920$ MeV, $5/2^+$ with $E^* = 0.921$ MeV, $5/2^+$ with $E^* = 1.089$ MeV and $5/2^+$ with $E^* = 1.354$ MeV). If the yields related to the $1/2^-$ ($E^* = 0.478$ MeV) excited state of the ^7Li ejectile are not negligible, they would be included inside Peak 2.

Coupled reaction channel (CRC) calculations were performed using the FRESKO code, adopting 150 partial waves. For the initial partition, $^6\text{Li} + ^{120}\text{Sn}$, we have adopted the same optical potentials as mentioned before. The calculations assumed the prior representation (complex remnant) since there is a higher degree of confidence of the optical potential adopted for the initial partition (as we may compare the data with the calculations). The optical potential chosen for the exit partition was the standard SPP considering $N_i = 0.78$ (one may observe in Refs. [13,43] that a good description of elastic data was achieved with this optical potential). This procedure is also in accordance with the fact that no couplings among the

TABLE I. Spectroscopic amplitudes used in the CRC calculations for one-neutron transfer reactions. The initial and final states of each transition are indicated, as also as nm , l , and j , which are the quantum numbers of the neutron/neutron orbitals for the reaction. The last column shows in which peak experimental peak each theoretical state have been included in order to be compared with data.

Initial	Final	nm	l	j	A_{lsj}	Peak
$^6\text{Li} - 1^+$	$^7\text{Li} - 3/2_1^-$	1	1	1/2	0.54	1
$^6\text{Li} - 1^+$	$^7\text{Li} - 3/2_1^-$	1	1	3/2	0.66	1
$^6\text{Li} - 1^+$	$^7\text{Li} - 1/2_1^-$	1	1	1/2	0.20	2
$^6\text{Li} - 1^+$	$^7\text{Li} - 1/2_1^-$	1	1	3/2	0.92	2
$^{120}\text{Sn} - 0^+$	$^{119}\text{Sn} - 1/2_1^+$	3	0	1/2	0.70	1
$^{120}\text{Sn} - 0^+$	$^{119}\text{Sn} - 3/2_1^+$	2	2	3/2	1.30	1
$^{120}\text{Sn} - 0^+$	$^{119}\text{Sn} - 11/2_1^-$	1	5	11/2	2.03	1
$^{120}\text{Sn} - 0^+$	$^{119}\text{Sn} - 7/2_1^+$	1	4	7/2	2.00	2
$^{120}\text{Sn} - 0^+$	$^{119}\text{Sn} - 3/2_2^+$	2	2	3/2	0.59	2
$^{120}\text{Sn} - 0^+$	$^{119}\text{Sn} - 5/2_1^+$	2	2	5/2	0.45	2
$^{120}\text{Sn} - 0^+$	$^{119}\text{Sn} - 5/2_2^+$	2	2	5/2	1.68	2
$^{120}\text{Sn} - 0^+$	$^{119}\text{Sn} - 5/2_3^+$	2	2	5/2	0.99	2

final partition states have been considered. The neutron-core potentials have been chosen to have a central real WS shape, with diffuseness $a = 0.60$ fm and two different values for the reduced radii: $r_0 = 1.2$ fm and $r_0 = 1.3$ fm. With this procedure, we can test the sensitivity of the transfer cross sections to the geometry of the neutron-core potentials. The depths of the WS potentials are adjusted to reproduce the experimental binding energies of the neutron-core participants. In addition, a spin-orbit component have also been included, with the usual derivative form factor and the same radius and diffuseness values assumed for the central part, with a fixed depth of 5 MeV. The spectroscopic amplitudes for each transition have already been studied in our previous works. The $^{119}\text{Sn} - ^{120}\text{Sn}$ transitions could be obtained from Refs. [21,46], while the $^6\text{Li} - ^7\text{Li}$ amplitudes and relevant quantum numbers were taken from [13]. The spectroscopic amplitudes adopted in this work present a variation of about 10% when compared to the previous ones. Such variation is compatible with the experimental errors of the experiments. The quantities necessary to describe the neutron wave function on each transition are given in Table I.

Figures 6, 7, and 8 present the experimental cross sections compared to the CRC theoretical calculations. The upper panels of Figs. 7 and 8 show the cross sections related to the first three low-lying states of ^{119}Sn , while the lower panels present the cross sections obtained from the yields of the second peak observed on the spectra. The states $7/2^+$ ($E^* = 0.787$ MeV) and the second $5/2^+$ ($E^* = 1.089$ MeV) are those which most contribute to the total cross section observed. For $E_{\text{lab}} = 19$ MeV, only the first three low-lying states of ^{119}Sn have been experimentally observed. The lines represent CRC results obtained as the sum of the contributions of each excited state of the ^{119}Sn nucleus. The different theoretical curves correspond to different initial partition and neutron-core potentials. Clearly, the theoretical cross sections are quite dependent on the choice of the parameter values for the potentials. In fact, such a dependence has already been

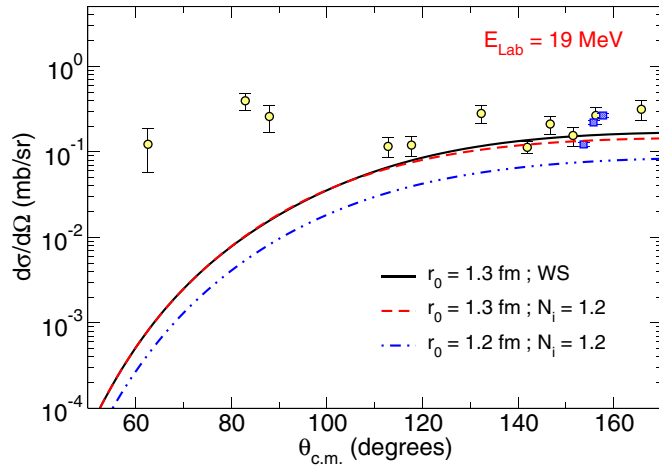


FIG. 6. One-neutron pickup transfer cross section for the ${}^6\text{Li} + {}^{120}\text{Sn}$ reaction at $E_{\text{lab}} = 19$ MeV. The SATURN and STAR data are represented by the yellow circles and blue squares, respectively. The solid black line in the figure was obtained from the CRC calculations as the sum of the states of ejectile and recoil nuclei labeled as Peak 1 in Table I.

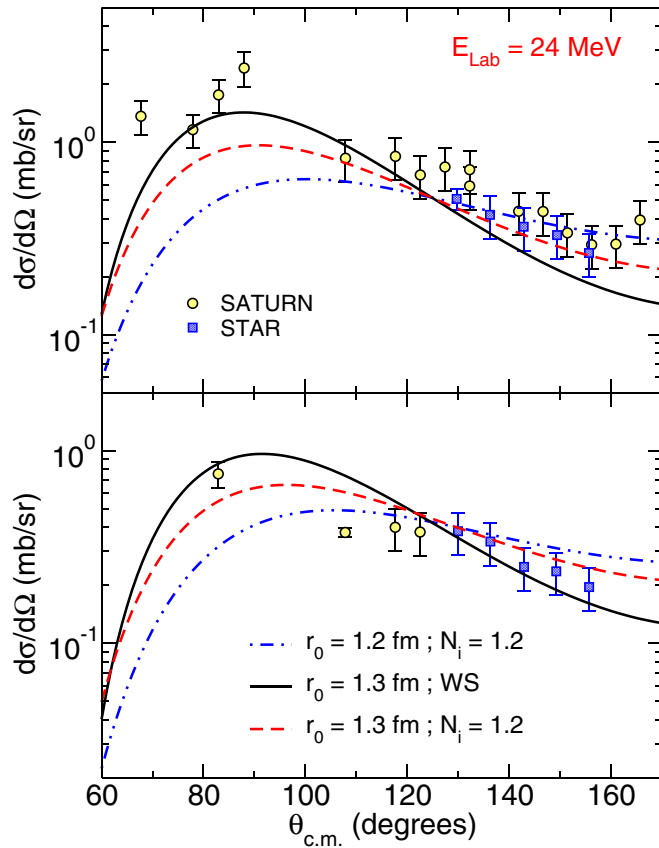


FIG. 7. The same as Fig. 6 but for 24 MeV. The upper panel shows the cross sections related to the first three low-lying states of ${}^{119}\text{Sn}$ (labeled as Peak 1 in Table I). The lower panel presents the cross sections obtained from the yields of the second peak observed on the spectra (labeled as Peak 2 in Table I).

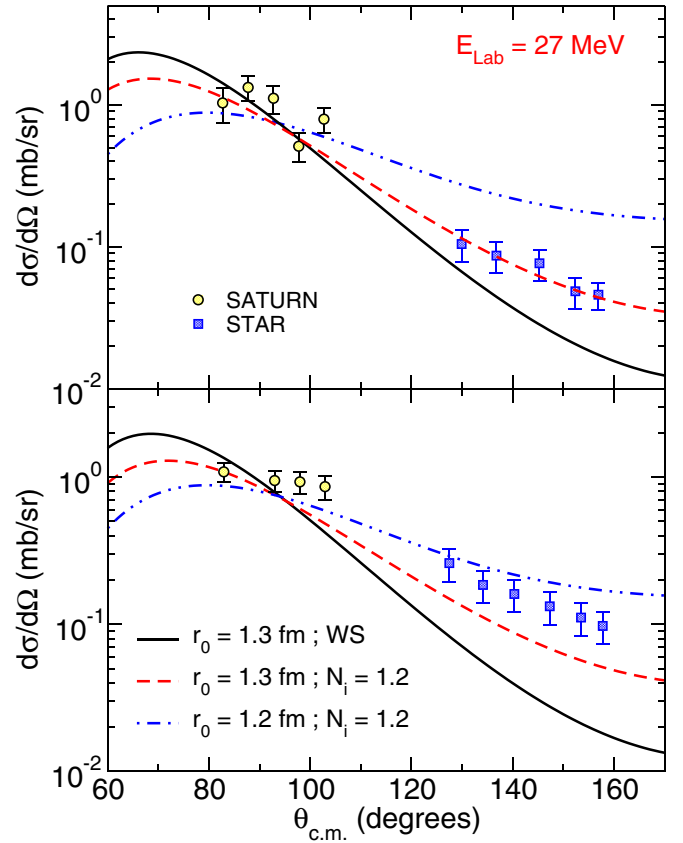


FIG. 8. The same as Fig. 7 for 27 MeV.

discussed in other papers (see, e.g., [21]). One may notice that the variation of the parameters may cause the redistribution of the probability flux, increasing the cross sections in a given angular region and diminishing it on others. The CRC angular distributions obtained with $r_0 = 1.3$ fm and $N_i = 1.2$ are in good agreement with the data, except at $E_{\text{lab}} = 19$ MeV for forward angles. The theoretical cross sections at this energy and angular region are about two orders of magnitude smaller than the data, indicating that the probability of observing events related to this channel in our experiment should be small. However, since the corresponding yields were obtained with single surface barrier detectors, the actually observed events might be associated to other processes lying in the same energy region of the spectra. It is important to mention that the couplings to the one-neutron transfer channel do not significantly affect the theoretical cross sections for the elastic and inelastic processes, which is a similar result obtained in Ref. [13].

In Ref. [47], it was shown that the one neutron stripping process, followed by the break up of the ${}^5\text{Li}$ ejectile, plays an important role for the incomplete fusion cross section. Unfortunately, such a reaction channel cannot be studied here from the experimental point of view, since coincidence measurements are required to obtain the ${}^5\text{Li}$ break-up cross sections. Additionally, it is difficult to include the one-neutron transfer plus the ${}^5\text{Li}$ break-up channel in the theoretical calculations performed in the present work.

IV. CONCLUSIONS

Several elastic, inelastic and transfer angular distributions have been measured for the ${}^6\text{Li} + {}^{120}\text{Sn}$ reaction at 19, 24, and 27 MeV bombarding energies. The experimental spectra display peaks which are kinematically compatible with the excitation of the first 2^+ and 3^- states of ${}^{120}\text{Sn}$. Besides them, it was possible to associate two observed peaks with the $1n$ -pickup process to different groups of ${}^7\text{Li}$ and ${}^{119}\text{Sn}$ states.

Several attempts to describe the data were performed using different theoretical approaches. One of them corresponds to CC calculations assuming the SPP for the real part of the optical potential, and an internal imaginary WS shape for the imaginary part. We have also performed CC calculations considering an imaginary potential obtained by scaling the real part by a factor $N_i = 1.2$, that corresponds to strong surface absorption. A third approach corresponds to CDCC calculations including projectile and target excitations. Finally, we included the one-neutron pickup channel transfer through CRC calculations.

The theoretical calculations describe reasonably well most of the complete elastic and inelastic scattering data sets corresponding to $E_{\text{lab}} = 24$ and 27 MeV, being the CDCC results slightly better than the CC ones. The description of the data at the sub-barrier energy of 19 MeV is more challenging. It is worth mentioning that the CDCC theoretical results provided the best description of the 3^- excitation data at 19 MeV. However, concerning the elastic scattering, the best theoretical result was obtained with the CC calculations based on the folding model with $N_i = 1.2$ approach. The corresponding strong surface absorption could be related to BU channel effects. However, the CDCC calculations underestimate the data at this low energy.

The disagreement between inelastic data of the 3^- target state and the theoretical results at forward angles may be

explained by a possible spurious contribution of the $3^+ {}^6\text{Li}$ resonant state to the experimental cross sections. More experimental data points at this forward angular region would be necessary to understand the origin of such discrepancy.

The theoretical one-neutron transfer cross sections depend strongly on the choice of the geometry assumed for the neutron-core potentials. We have obtained a satisfactory data description for this channel in the context of the CRC calculations with a strong absorptive imaginary potential for the initial partition ($N_i = 1.2$), and $r_0 = 1.3$ fm for the radii of the neutron-core WS potentials. Nevertheless, this theoretical results are orders of magnitude smaller than the data for forward angles at $E_{\text{lab}} = 19$ MeV. We are not sure about the origin of this discrepancy, which might be related to spurious contributions of other processes to the observed yields.

ACKNOWLEDGMENTS

V.A.B.Z, L.R.G., L.C.C., A.L.Z., V.S., and J.R.B.O. were supported by FAPESP (Proc. No 2019/07767-1), FAPERJ, CAPES, CNPq, and INCT-FNA (Instituto Nacional de Ciência e Tecnologia-Física Nuclear e Aplicações) (Proc. No. 464898/2014-5). This work was also partially supported by the Ministry of Science, Innovation and Universities of Spain (Proc. No. PGC2018-096994-B-C21). M.G.R., A.M.M., J.P.F.G., M.A.G.A. are supported by the grant Group FQM-160 and the project PAIDI 2020 with Ref. P20_01247, funded by the Consejería de Economía, Conocimiento, Empresas y Universidad, Junta de Andalucía (Spain) and by “ERDF A way of making Europe”. We would also like to thank the technical staff of LAFN for assisting in the maintenance and operation of the accelerator.

-
- [1] A. Coc., S. Goriely, Y. Xu, M. Saimpert, and E. Vangioni, *Astrophys. J.* **744**, 158 (2012).
- [2] D. Trezzi, M. Anders, M. Aliotta, A. Bellini, D. Bemmerer, A. Boeltzig, C. Broggini, C. G. Bruno, A. Caciolli, F. Cavanna *et al.*, *Atrop. Phys.* **89**, 57 (2017).
- [3] P. A. R. Ade, P. A. R. Ade, N. Aghanim, Y. Akrami, M. I. R. Alves, F. Argüeso, M. Arnaud, F. Arroja, M. Ashdown, J. Aumont, C. Baccigalupi *et al.*, *Astron. Astrophys.* **594**, A4 (2016).
- [4] B. D. Fields, *Annu. Rev. Nucl. Part. Sci.* **61**, 47 (2011).
- [5] R. H. Cyburt, J. Ellis, B. B. Fields *et al.*, *J. Cosmol. Astropart. Phys.* **2013**, 014 (2013).
- [6] M. Asplund, D. L. Lambert, P. E. Nissen, F. Primas, and V. V. Smith, *Astrophys. J.* **644**, 229 (2006).
- [7] F. Spite and M. Spite, *Astron. Astrophys.* **115**, 357 (1982).
- [8] F. Matteucci, M. Molero, D. S. Aguado, and D. Romano, *Mon. Not. R. Astron. Soc.* **505**, 200 (2021).
- [9] P. D. Serpico, S. Esposito, F. Iocco, G. Mangano, G. Miele, and O. Pisanti, *J. Cosmol. Astropart. Phys.* **2004**, 010 (2004).
- [10] J. Rangel, M. R. Cortes, J. Lubian, and L. F. Canto, *Phys. Lett. B* **803**, 135337 (2020).
- [11] M. Dasgupta, D. J. Hinde, K. Hagino, S. B. Moraes, P. R. S. Gomes, R. M. Anjos, R. D. Butt, A. C. Berriman, N. Carlin, C. R. Morton *et al.*, *Phys. Rev. C* **66**, 041602(R) (2002).
- [12] C. L. Guo, G. L. Zhang, S. P. Hu, J. C. Yang, H. Q. Zhang, P. R. S. Gomes, J. Lubian, X. G. Wu, J. Zhong, C. Y. He *et al.*, *Phys. Rev. C* **92**, 014615 (2015).
- [13] V. A. B. Zagatto, J. Lubian, L. R. Gasques, M. A. G. Alvarez, L. C. Chamon, J. R. B. Oliveira, J. A. Alcántara-Núñez, N. H. Medina, V. Scarduelli, A. Freitas, I. Padron, E. S. Rossi, Jr. and J. M. B. Shorto, *Phys. Rev. C* **95**, 064614 (2017).
- [14] J. C. Zamora, V. Guimarães, A. Barioni, A. Lépine-Szily, R. Lichtenthäler, P. N. de Faria, D. R. Mendes Jr., L. R. Gasques, J. M. B. Shorto, V. Scarduelli, K. C. C. Pires, V. Morcelle, E. Leistenschneider, R. P. Condori, V. A. Zagatto, M. C. Moraes, and E. Crema, *Phys. Rev. C* **84**, 034611 (2011).
- [15] D. Martínez Heimann, A. J. Pacheco, O. A. Capurro, A. Arazi *et al.*, *AIP Conf. Proc.* **1423**, 109 (2012).
- [16] S. Kalkal, E. C. Simpson, D. H. Luong, K. J. Cook, M. Dasgupta, D. J. Hinde, I. P. Carter, D. Y. Jeung, G. Mohanto, C. S. Palshetkar, E. Prasad, D. C. Rafferty, C. Simenel, K. Vo-Phuoc, E. Williams, L. R. Gasques, P. R. S. Gomes, and R. Linares, *Phys. Rev. C* **93**, 044605 (2016).

- [17] N. Austern, Y. Iseri, M. Kamimura, M. Kawai, G. Rawitscher, and M. Yahiro, *Phys. Rep.* **154**, 125 (1987).
- [18] J. A. Tostevin, S. Rugmai, and R. C. Johnson, *Phys. Rev. C* **57**, 3225 (1998).
- [19] E. O. Alt, P. Grassberger, and W. Sandhas, *Nucl. Phys. B* **2**, 167 (1967).
- [20] V. A. B. Zagatto, J. R. B. Oliveira, L. R. Gasques, J. A. Alcántara-Núñez, J. G. Duarte, V. P. Aguiar, N. H. Medina, W. A. Seale, K. C. C. Pires, and A. Freitas, *J. Phys. G: Nucl. Part. Phys.* **43**, 055103 (2016).
- [21] L. R. Gasques, A. S. Freitas, L. C. Chamon, J. R. B. Oliveira, N. H. Medina, V. Scarduelli, E. S. Rossi, Jr. M. A. G. Alvarez, V. A. B. Zagatto, J. Lubian, G. P. A. Nobre, I. Padron, and B. V. Carlson, *Phys. Rev. C* **97**, 034629 (2018).
- [22] M. A. G. Alvarez, M. Rodríguez-Gallardo, L. R. Gasques, L. C. Chamon, J. R. B. Oliveira, V. Scarduelli, A. S. Freitas, E. S. Rossi, Jr. V. A. B. Zagatto, J. Rangel, J. Lubian, and I. Padron, *Phys. Rev. C* **98**, 024621 (2018).
- [23] L. R. Gasques, M. A. G. Alvarez, A. Arazi, B. V. Carlson, L. C. Chamon, J. P. Fernández-García, A. Lépine-Szily, J. Lubian, J. Rangel, M. Rodríguez-Gallardo, V. Scarduelli, and V. A. B. Zagatto, *Phys. Rev. C* **103**, 034616 (2021).
- [24] L. R. Gasques, L. C. Chamon, A. Lépine-Szily, V. Scarduelli, V. A. B. Zagatto, D. Abriola, A. Arazi, M. A. Cardona, E. de Barbará, J. de Jesús *et al.*, *Phys. Rev. C* **101**, 044604 (2020).
- [25] M. A. G. Alvarez, J. P. Fernández-García, J. L. León-García, M. Rodríguez-Gallardo, L. R. Gasques, L. C. Chamon, V. A. B. Zagatto, A. Lépine-Szily, J. R. B. Oliveira, V. Scarduelli, B. V. Carlson, J. Casal, A. Arazi, D. A. Torres, and F. Ramirez, *Phys. Rev. C* **100**, 064602 (2019).
- [26] N. C. Summers, F. M. Nunes, and I. J. Thompson, *Phys. Rev. C* **74**, 014606 (2006).
- [27] R. de Diego, J. M. Arias, J. A. Lay, and A. M. Moro, *Phys. Rev. C* **89**, 064609 (2014).
- [28] A. Deltuva, *Phys. Rev. C* **88**, 011601(R) (2013).
- [29] M. Yahiro, Y. Iseri, H. Kameyama, M. Kamimura, and M. Kawai, *Prog. Theor. Phys. Suppl.* **89**, 32 (1986).
- [30] H.-T. Pierre Chau and H. Tai, *Eur. Phys. J. A* **51**, 166 (2015).
- [31] M. Gómez-Ramos and A. M. Moro, *Phys. Rev. C* **95**, 034609 (2017).
- [32] A. Woodard, J. Figueira, D. Otomar, J. F. Niello, J. Lubian, A. Arazi, O. Capurro, P. Carnelli, L. Fimiani, G. Mart *et al.*, *Nucl. Phys. A* **873**, 17 (2012).
- [33] E. Muskat, J. Carter, R. Fearick, and V. Hnizdo, *Nucl. Phys. A* **581**, 42 (1995).
- [34] V. Scarduelli, L. R. Gasques, L. C. Chamon, and A. Lépine-Szily, *Eur. Phys. J. A* **56**, 24 (2020).
- [35] A. Arazi, J. Casal, M. Rodríguez-Gallardo, J. M. Arias, R. Lichtenthaler Filho, D. Abriola, O. A. Capurro, M. A. Cardona, P. F. F. Carnelli, E. de Barbara, J. Fernandez Niello, J. M. Figueira, L. Fimiani, D. Hojman, G. V. Martí, D. Martinez Heimman, and A. J. Pacheco, *Phys. Rev. C* **97**, 044609 (2018).
- [36] M. A. Cândido Ribeiro, L. C. Chamon, D. Pereira, M. S. Hussein, and D. Galetti, *Phys. Rev. Lett.* **78**, 3270 (1997).
- [37] L. C. Chamon, D. Pereira, M. S. Hussein, M. A. Candido Ribeiro, and D. Galetti, *Phys. Rev. Lett.* **79**, 5218 (1997).
- [38] L. C. Chamon, B. V. Carlson, L. R. Gasques, D. Pereira *et al.*, *Phys. Rev. C* **66**, 014610 (2002).
- [39] S. Raman, C. W. Nestor, and P. Tikkanen, *At. Data Nucl. Data Tables* **78**, 1 (2001).
- [40] D. S. Andreev, V. D. Vasilev, G. M. Gusinskii, K. I. Erokhina, and I. K. Lemberg, *Izvest. Akad. Nauk SSSR, Ser. Fiz.* **832**, 25 (1961); *Columbia Tech. Transl.* **842**, 25 (1962).
- [41] T. Kibédi and R. H. Spear, *At. Data Nucl. Data Tables* **80**, 35 (2002).
- [42] I. J. Thompson, *Comput. Phys. Rep.* **7**, 167 (1988).
- [43] M. A. G. Alvarez, Jr. L. C. Chamon, M. S. Hussein, D. Pereira, L. R. Gasques, E. S. Rossi, Jr. and C. P. Silva, *Nucl. Phys. A* **723**, 93 (2003).
- [44] W. W. Daehnick, J. D. Childs, and Z. Vrcelj, *Phys. Rev. C* **21**, 2253 (1980).
- [45] S. Watanabe, T. Matsumoto, K. Takuma, K. Ogata, and M. Yahiro, *Phys. Rev. C* **86**, 031601(R) (2012).
- [46] S. A. Dickey, J. J. Kraushaar, R. A. Ristinen, and M. A. Rumore, *Nucl. Phys. A* **377**, 137 (1982).
- [47] A. Diaz-Torres and D. Quraishi, *Phys. Rev. C* **97**, 024611 (2018).